# Combined InSAR and Terrestrial Structural Monitoring of Bridges

Sivasakthy Selvakumaran, *Student Member, IEEE,* Cristian Rossi, Andrea Marinoni, *Senior Member, IEEE*, Graham Webb, John Bennetts, Elena Barton, Simon Plank, and Campbell Middleton

***Abstract*—This paper examines advances in InSAR satellite measurement technologies to understand their relevance, utilisation and limitations for bridge monitoring. Waterloo Bridge is presented as a case study to explore how InSAR data sets can be combined with traditional measurement techniques including sensors installed on the bridge and automated total stations. A novel approach to InSAR bridge monitoring was adopted by the installation of physical reflectors at key points of structural interest on the bridge, in order to supplement the bridge's own reflection characteristics and ensure that the InSAR measurements could be directly compared and combined with in-situ measurements. The interpretation and integration of InSAR data sets with civil infrastructure data is more than a trivial task, and a discussion of uncertainty of measurement data is presented. Finally, a strategy for combining and interpreting varied data from multiple sources to provide useful insights into each of these methods is presented, outlining the practical applications of this data analysis to support wider monitoring strategies.**

***Index Terms*—structural health monitoring, bridge, Interferometric synthetic aperture radar (InSAR), TerraSAR-X, corner reflectors.**

## I. Introduction

THE ageing and deterioration of bridge structures has highlighted the value of developing structural monitoring systems to protect our built environment. Collapses of bridges in recent years are evidence of the safety-critical nature of this topic, but there are also great advantages in spotting signs of deterioration and unusual behaviours in functioning bridges. Periodic visual inspection of bridges is the primary means used by asset managers to assess the current condition of bridge assets, however this approach has significant challenges.

Several studies have shown that there is considerable subjectivity and variation in the recording of defects between individual inspectors when inspecting the same asset [1], [2]. A balance also needs to be struck between having regular asset monitoring and the cost of doing so, financially as well as with regards to the disruption caused to the network (e.g. by bridge closure). Consequently, inspections are typically carried out every few years (for example, General Inspections, relying on visual observations, are expected to be carried out every 2 years whilst Principal Inspections at touching distance of highway structures in the UK are carried out every 6 years [3]). It has been acknowledged that structural health monitoring (SHM) making use of technology to take more frequent readings can provide more objective and repeatable data to supplement visual inspections [4], [5].

One such technology is satellite radar imagery, which is becoming more accessible, and at increasing spatial and time resolutions. Notably, radar imagery taken by satellites can be used to monitor millimetre-scale movements of built environment assets over time by exploiting the principles of radar interferometry [6]–[8]. In urban contexts, the reliability of coherent targets known as persistent scatterers (PSs) are used to monitor various effects related to structural health [9]–[11]. Within the asset management context outlined, InSAR provides the opportunity to collect readings related to bridge movement, and in an interval period of days. Thus, there are opportunities in being able to monitor for signs of unusual behaviour that develop in the periods between inspections or are not picked up visually. This can provide a means of remote monitoring which covers large geographical regions and insights into infrastructure assets that are difficult to access or regularly monitor with conventional approaches. InSAR monitoring offers a further advantage over traditional sensor monitoring in that it does not require an electrical connection or power source at site, or closure and physical access to the bridge.

There are many studies in the literature illustrating the value of using InSAR in city monitoring. In the last few decades, monitoring of ground subsidence over city-scale areas [12] has highlighted the effects of anthropogenic actions such as monitoring movements due to ground water exploitation [13], mining activities [14] and oil and gas extraction [15].The technique can make use of surface level deformations to understand subterranean infrastructure activities such as tunnelling, by measuring settlement resulting from the tunnelling process [16], [17]. Considering InSAR to monitor surface assets themselves, examples such as [9] uses InSAR to assess the structural condition and risk to buildings in the historic centre of Rome, Italy, and [18] uses InSAR to detect and monitor small changes in buildings situated on reclaimed land to assess potential damage to structures. A brief review of InSAR methodologies, limitations and key applications is provided by [19].

On the topic of bridge monitoring, the literature provides evidence that InSAR can be used to monitor different features of bridge behaviour, such as ground settlement at pier locations

S. Selvakumaran and C. Middleton are with the Department of Engineering, University of Cambridge, United Kingdom,e-mail: (sakthy@cantab.net).

C. Rossi is with Satellite Applications Catapult, UK.

A. Marinoni is with Dept. of Physics and Technology, UiT The Arctic University of Norway, NO-9037, Tromsø, Norway.

G. Webb and J. Bennetts are with WSP UK.

E. Barton is with the National Physical Laboratory, UK.

S. Plank is with German Remote Sensing Data Center, German Aerospace Center (DLR), Oberpfaffenhofen, Germany.

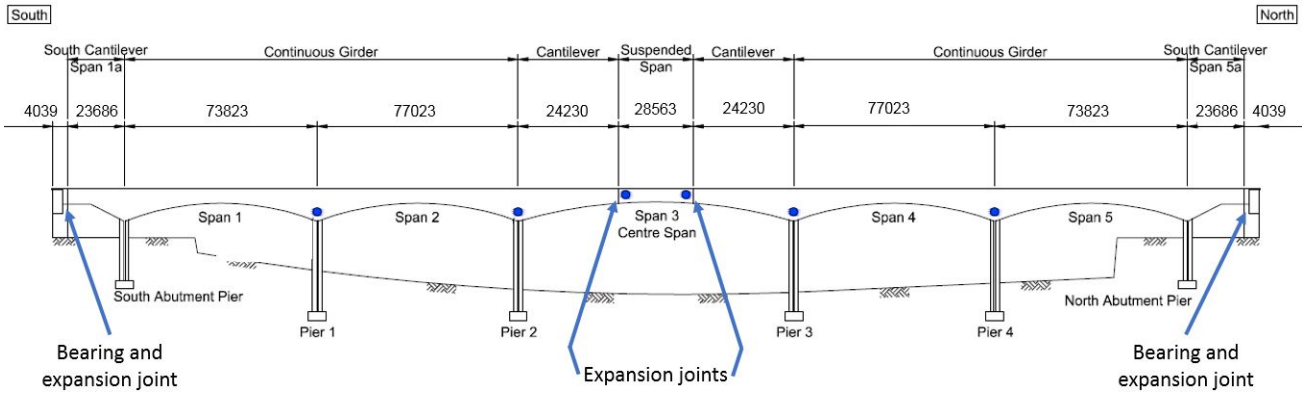


Fig. 1. Structure of Waterloo Bridge. ATS prisms and corner reflector locations are marked as blue dots.

or seasonal thermal expansion [20], [21]. InSAR has also been used to study collapsed structures to show how the technique could be used to detect precursor signs of failure [22], [23]. Many of the bridge structures studied in the literature focus on the interpretation of SAR measurements, or study of ground subsidence in the area, often without comparison with in-situ measurement data of movement from the bridge itself to validate the readings.

In this paper Waterloo Bridge, over the River Thames in London, is presented as a case study to investigate the potential for using InSAR satellite monitoring data to support bridge management activities. Section I introduces the topic of InSAR for bridge monitoring and Section II discusses Waterloo Bridge. Corner reflectors and target prisms for automated total station (ATS) measurements were installed at key points of interest as part of a wider structural monitoring system, as outlined in Section III, and the methods used for data processing are presented in Section IV. Section V presents the results of this processing and the displacement data from the SAR and ATS systems are compared and studied to gain a better understanding of measurement uncertainty and the relationship between the datasets. Section VI investigates how the two methods of measurement could be combined to enhance the robustness of the measurements before finally presenting conclusions in Section VII.

## II. Bridge structure

Waterloo Bridge is a 434m concrete bridge carrying the A301 across the River Thames in London [24]. The bridge comprises two reinforced concrete, multi-cell box girders and a concrete deck. It has five main spans and is nominally symmetric about its centreline (Figure 1). In each half the box girders and deck are continuous over two spans, with cantilever projections beyond the abutment piers and into the central span, where they support a central drop-in section. In 1981 the bridge was designated as a Grade II* Listed structure by Historic England.

The bridge responds to changes in temperature by expanding or contracting over its 434m length. This daily and seasonal change in length of the structure is accommodated through four expansion joints, one at each abutment at either end of the bridge and one at each end of the central drop-in span. Recent inspections have revealed a number of concerns relating to the performance of the bridge's articulation, prompting further work to investigate the bridge's current condition and develop potential remedial solutions if necessary.

The roller bearings supporting the bridge's central drop-in span are unusual in design. Recent inspections have highlighted significant deterioration. There are concerns that the bearings and lateral restraint members across the joints may have locked up due to corrosion, silt build-up, and dislodged components. If true, this would have the consequential effect of changing the bridge's articulation, introducing additional stresses into the structure's deck and piers when the bridge expands and contracts due to temperature variations. The approach slabs at both ends of the bridge are supported by bearings on the ends of the approach viaducts. The original segmental roller bearings at the north and south abutments were replaced with elastomeric bearing pads in 2006 and 2010 respectively. However, some of the replacement bearings have themselves failed and displaced from their supports, suggesting that they are experiencing movement ranges greater than expected during their design. It is likely that the bridge's approach viaducts will also respond to temperature changes and may therefore be contributing to the failure of the elastomeric bearings.

## III. Experimental set up

### A. Traditional monitoring

An automated monitoring system made up of 48 temperature sensors (located at multiple points along the length as well as through the deck at top, middle and bottom of the concrete section), and 20 displacement transducers (at the bearing and expansion joint locations) was installed within the bridge deck in December 2017. Measurements from these temperature and displacement gauges were taken simultaneously every 1 second.

In addition, two Automated Total Stations (ATS) were installed looking at either side of the bridge to monitor 12 reflective prisms. Six prisms were installed to each side of the structure (at each of the bridge's river piers, and one at each end of the central drop-in span, marked as dots in Figure 1).

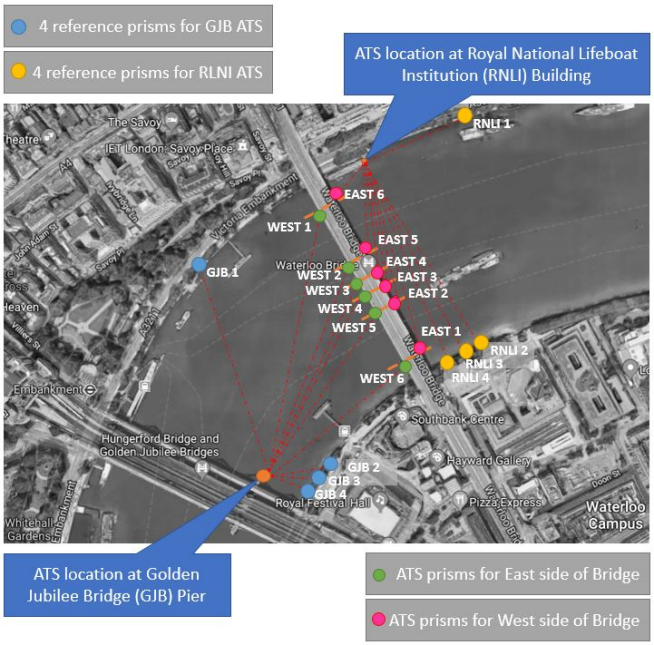


Fig. 2. ATS locations, target prism locations on the bridge and reference prism locations on the embankments (base optical imagery and map data provided by Google (2019).

Eight additional prisms were installed as reference points at positions which are not located on the bridge structure, but on adjacent sites on the River Thames embankment (Figure 2). ATS readings were taken every 5 minutes.

Tidal data for the duration of the monitoring period was provided by the Port of London Authority. The river water levels for the London Bridge gauge were used.

### *B. Satellite data sets*

TerraSAR-X Stripmap mode images (approximately 3m by 3m ground resolution) were tasked for acquisitions every 11 days in both ascending and descending directions from December 2017 until November 2018. 30 images in the ascending mode and 30 images in descending mode were used to process the time series movement of the corner reflectors.

Shuttle Radar Topography Mission (SRTM) data with resolution of 3 arc-second (90m) was used as a Digital Elevation Model (DEM) during the interferometric processing.

### *C. Corner reflectors*

Corner reflectors can be used to create points that are easy to identify within SAR imagery by increasing reflected amplitude of the signal at the location where they are installed. These stable reflective points can then be used as Persistent Scatterers (PS). The SAR image of Waterloo Bridge was assessed prior to the installation of corner reflectors. It was noted that the concrete structure of the bridge provided few natural PS, and the noise of the signal from other points on the bridge was relatively low. The absence of other PS prior to corner reflector installation meant that the new PS after installation could be attributed to the corner reflectors (without ambiguity that the response was coming from another object). The low noise


Fig. 3. Top image is a photo of the west side of Waterloo Bridge as taken from Golden Jubilee Bridge. Bottom image is a photo of East 6 aluminium corner reflector (circled) installed on bridge pier alongside ATS prism target.

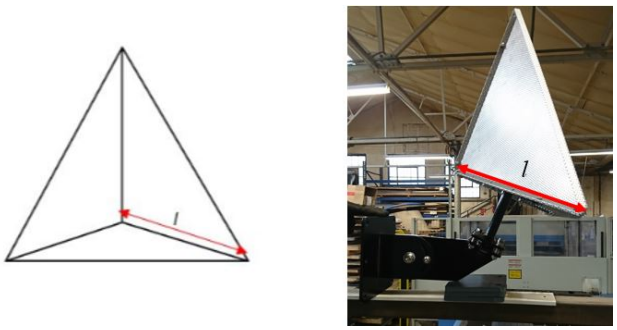


Fig. 4. Trihedral corner reflector shape where 'l' the dimension of the interior edge used in the RCS calculation for reflectivity.

level was advantageous as the response of any installed corner reflectors would be able to be seen as clear and distinguishable above other noise and clutter. The corner reflector was sized in terms of its radar cross section (RCS), a measure of the reflectivity, such that the reflected signal would be significantly higher than the background clutter, but small enough to gain permission from the bridge owner so that it could be mounted on the bridge (Figure 3). The corner reflectors used had a corner length, $l$ of 35cm, where $l$ is the length of the non-hypotenuse sides of the right-angled isosceles triangular plate (Figure 4).

The corner reflector material was chosen to be aluminium, given that it is light weight and less susceptible to corrosion than steel. Pre-fabricated perforated sheeting was chosen to facilitate drainage, reduce wind load and reduce overall weight. In total, 12 corner reflectors were installed alongside each ATS prism location on the bridge (Figure 5). The reflectors were

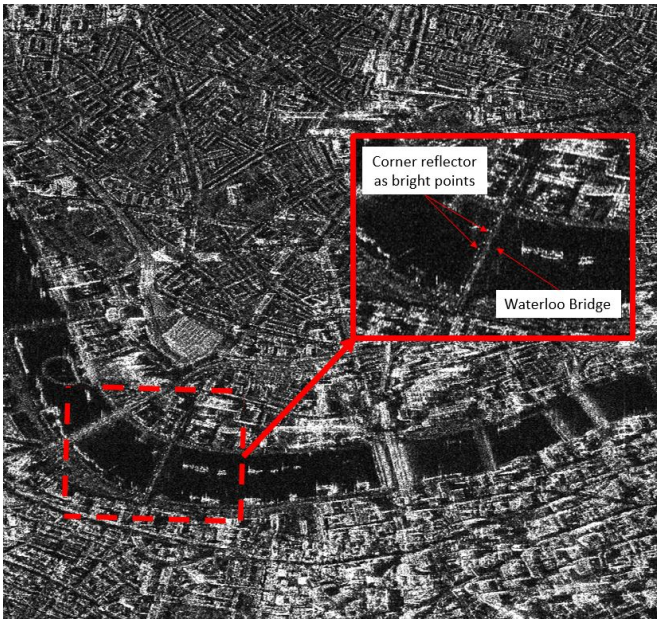


Fig. 5. Annotated SAR amplitude image with bridge marked and corner reflector installation appearing as bright points. This SAR image is a TerraSAR-X stripmap descending image taken 29th December 2017.

orientated such that the azimuth and elevation of each corner reflector was directed in the SAR satellite's line of sight (LOS) [25]. This was done to target the ascending pass on the west side of the bridge and the descending on the east.

## IV. Methods

### A. Data processing of in-situ data

The ATS monitoring system was designed to take line of sight distance readings to all bridge prisms, as well as to a number of points remote from the bridge (four points for each of the two ATS). The concept behind this is to find readings of bridge movement, relative to stable reference points. Doing so enables bridge movements to be distinguished from any movements of the abutments or approach viaducts (which could not be instrumented with displacement gauges). Raw data from the ATS monitoring system comprised angle and distance measurements from each of the ATS locations to the corresponding prisms. Every 2 hours each ATS observed each of its four reference prisms. Assuming that the coordinates of the reference prisms were fixed, the ATS calculated its position and then each prism's position at that moment. Due to measurement errors the angle and distance measurements from the four reference prisms did not all result in the same answer, so a Least Squares adjustment was carried out to select the most likely position. Every 5 minutes the ATS observed each of the bridge monitoring prisms and calculated their coordinates relative to its current location.

The reference prisms were installed on the river walls adjacent to the bridge. The river walls elsewhere in central London are known to be affected by the height of the tide. Figure 6 shows the variation with time of the measured distance between reference points on opposite sides of the river. Points RNLI RF1 and RNLI RF2 are to the East of the

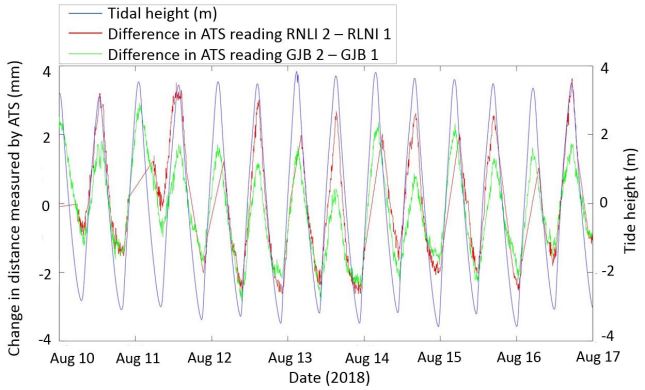


Fig. 6. Plot showing distance across river between north and south river walls over time. River reference prism data plotted in red and green; Tide data (plotted in blue) provided by London Port Authority for gauge at London Bridge.

bridge, and points GJB RF1 and GJB RF2 are to the West of the structure (refer to Figure 2 for locations). Also shown is the predicted tidal height. Since movements of the river walls appear to be similar in magnitude to movements of some parts of the bridge it is not possible to remove the effects of this error from the data, hence the absolute coordinates of all ATS monitoring prisms cannot be relied upon.

The initial processing method for the ATS data assumed that the reference prisms were stationary, which is not true and would report false results. Thus, for interpretation of bridge movement, the reported coordinates for each set of readings from the ATS have first been shifted so that the origin of each coordinate system is located at the prism at the south end of the bridge and the reported coordinates have been rotated such that the relative movements of all points (including both monitoring and reference prisms) can be determined longitudinally and transversely to the bridge.

### B. Data processing of SAR data

The principle of SAR interferometry (InSAR) is to compare the phase of two or more complex radar images for a given scene that have been acquired from slightly different positions (for the purpose of generating digital elevation models) or at different times (as in this case, for the purpose of monitoring movement over time) [6], [26]. Stacks of SAR data over the same area acquired at different times can be used to monitor millimetre-scale movements over a period of time.

Several approaches have been developed in the literature in order to extract information about these movements, but for the purpose of processing the SAR data in this study, Persistent Scatterer Interferometry (PSI) was employed. This technique uses reflectors (natural or otherwise) whose response to the radar is dominated by a strong reflecting object and is constant over time. A procedure for the identification and exploitation of stable permanent scatterers was developed by Ferretti et al. [7]. The technique relies on analysing pixels which remain stable, or coherent, over a sequence of interferograms. This approach was selected in preference to those based on the analysis of distributed scatterers [27] as the points of interest

were clearly identifiable point targets created by the installation of corner reflectors. A stack of acquisitions each of the ascending and descending pass directions was processed.

## V. Results

The processing of stacks of images collected after the installation of the corner reflectors identified some new persistent scatterers compared to images processed prior to installation, which can be attributed the corner reflectors. However, 3 of the 12 corner reflector locations are missing persistent scatterer points. Possible reasons include a reflector becoming dirty or events such as a bird nesting in the corner. Although the latter issue was not visible during on-site inspections, one reflector did have litter thrown into it. The PSI processing resulted in LOS displacements over time for 4 out of 6 corner reflector locations on the East side and 5 out of 6 corner reflector locations on the West side (Figure 8). The temporal coherence values of these PS were all between 0.77 to 0.81 apart from the PS attributed to East 6 which had a slightly lower coherence of 0.71.

The PSI processing output on first glance would suggest that these PS are not all located on the bridge but in the near environment. However, we have already established that there was an absence of PS before installation, meaning that these PS can be attributed to known locations on the bridge. The reason for the discrepancy in the PSI output is to geolocation accuracy [28] as well as the fact that these PS are not located on the top of the bridge deck itself, but further down at the top of the piers. They would thus be affected by SAR imaging geometry effects such as layover and multiple bounces of the emitted SAR waves before returning to be received by the SAR sensor [29].

### A. Resolving in one direction

Measurements in the LOS direction are not a particularly useful quantity from the structural engineering point of view. In terms of bridge movement, we are primarily concerned with movements within the bridge's own reference system: longitudinal and transverse expansion, vertical movement, and any rotation.

It is worth noting that deformation is measured in a direction perpendicular to the satellite path, also called line-of-sight (LOS). The near-polar nature of the satellite orbits means there are limitations on what types of deformations can be measured. Any component of ground deformation oriented in direction along the satellite orbit path will not result in motion towards or away from the satellite sensor, and thus, as the angle between the satellite path and the bridge tends towards zero, the sensitivity of InSAR measurement towards movement in the bridge longitudinal direction tends towards zero.

Mathematically, the line of sight movement we have measured using SAR ($d_{LOS}$) can be considered as Equation (1).

$$d_{LOS} = \underline{A}\underline{y}^T \tag{1}$$

where

$$\underline{A} = [(cos\theta \quad sin\theta cos\alpha \quad sin\theta sin\alpha)] \tag{2}$$

$$\underline{y} = [(d_V \quad d_L \quad d_T)] \tag{3}$$

$\alpha$ is the heading angle relative to the bridge (angle of the SAR satellite flight path, Figure 9), $\theta$ is the incidence angle (angle between the SAR beam and the vertical, Figure 10), and $d_V$, $d_L$, and $d_T$ refer to the vertical, longitudinal and transverse components of the movement vector respectively.

Bridges are affected by numerous different loading scenarios which could cause deformation. Applied loads include traffic loading, wind loading, tidal loading and thermal loading. Additional activities in the area around the bridge could cause other movements, for example settlement induced by tunneling. The displacements induced by many of these are not possible to detect using InSAR as they occur more frequently than the repeat acquisition period. Construction activities in the area were noted during the study (e.g. tunneling work and the construction of new shafts) and access to the construction monitoring data confirmed that these works were far enough away as to not impact Waterloo Bridge during the study.

In order to compare equivalent data sets, it was initially assumed that all bridge movement only occurred in the longitudinal direction (the direction along the bridge from one river embankment to the other). By applying loading envelopes of various load scenarios into a structural model of the bridge (created using the finite element package LUSAS) it was found that the predominant loading case, causing the largest movements, would be in the longitudinal direction due to thermal expansion. With this initial assumption, the relationship between the line of sight (LOS) displacements and those in the bridge longitudinal direction was derived using the geometry in Figure 9.

As explained in Section IV-A, only relative longitudinal movements measured by the ATS could be relied upon, and in this case these were taken relative to the southern end of the bridge (ATS prisms at West 6 (W6) and East 1 (E1) locations). For an equivalent comparison, the longitudinal components of the LOS movements were calculated, and the measurements at locations W6 and E1 were subtracted for the west and east readings respectively.

When plotting the ATS- and SAR-derived longitudinal movements as well as temperature over time (such as the example in Figure 7), the seasonal variation seen in the SAR readings over the year matches the overall temperature profile and agrees with the ATS readings. However, on looking at the direct comparison of points (selecting the ATS readings at the time of SAR acquisition) there is deviation between the two readings. The correlation coefficient of relative ATS measurement against relative SAR movement varies from 0.41 to 0.76. This does show that the readings are positively correlated, to a reasonable to strong degree. Examining the plots themselves (Figure 11) reveals that the profiles correlate well for the beginning part of the time period considered. However, the two sets of values begin deviating from each other in May and they begin converging again in October. The reason for the discrepancy in trend, visible from May 2018 onward, is difficult to assess. A plausible explanation might be a phase unwrapping error, i.e. a processing error

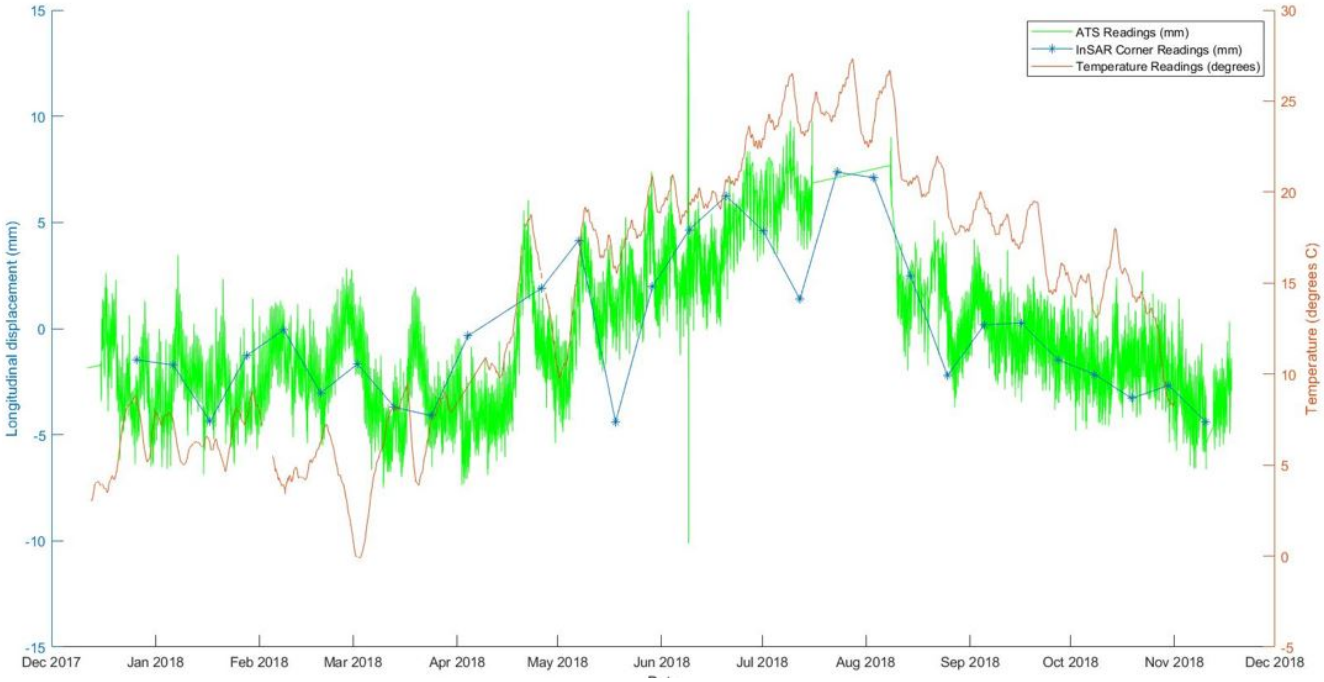


Fig. 7. Plot of relative ATS and SAR movements for Pier location 2 relative to Pier location 6 on the east side of the bridge.

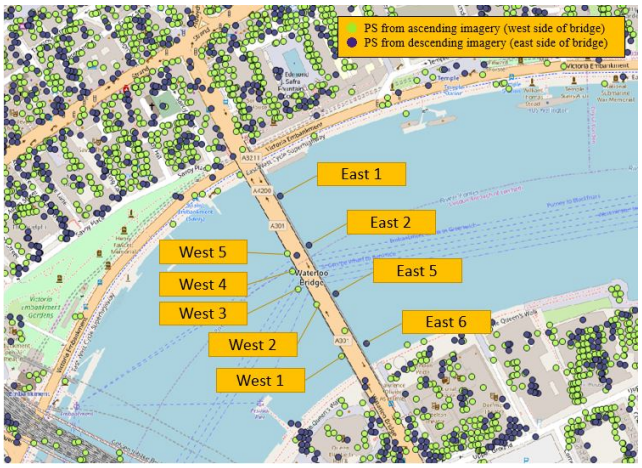


Fig. 8. Satellite monitoring data points (green dots indicate persistent scatterers derived from the TerraSAR-X data stack taken in an 'ascending' direction and blue dots indicate persistent scatterers derived from the TerraSAR-X data stack taken in a 'descending' direction.

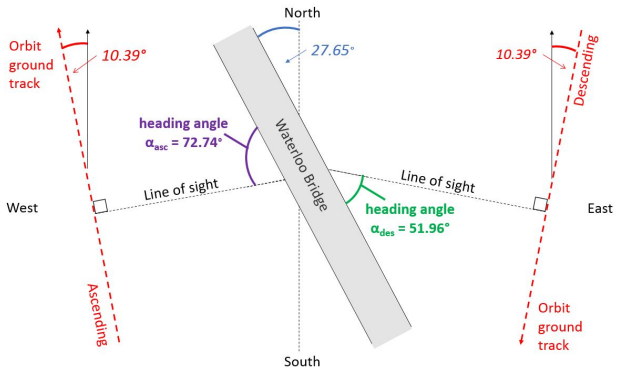


Fig. 9. Bridge orientation in relation to satellite imaging geometry.

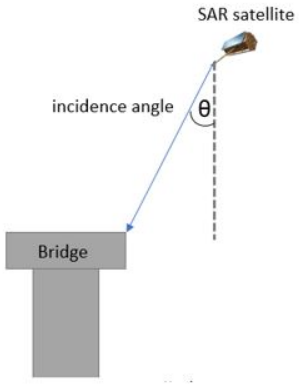


Fig. 10. Bridge orientation in relation to satellite imaging geometry.

occurring due phase aliasing which affects the trend of the measurements with a shift. Phase unwrapping errors are likely to occur for rapid motion and gaps in the data and can be corrected post-processing by an operator when independent measures are available. In the TerraSAR-X case, movements larger than 7.7mm between acquisitions may be subject of unwrapping errors.

This would suggest that this simple measure of uncertainty is not ideally suited to understand the complex data profile being considered. Therefore another means of assessing the fit between ATS and SAR measurements will be considered in Section V-C.

### *B. Using multiple look directions*

Several approaches have been developed in recent years to exploit the potential of InSAR to determine 3-D surface

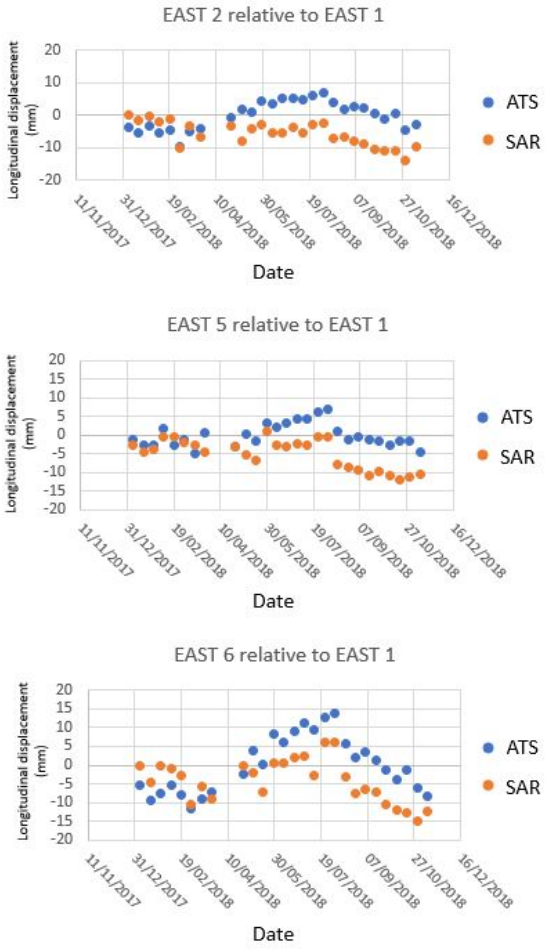


Fig. 11. Comparison between relative ATS and SAR longitudinal measurements at various locations on the bridge.

displacement [30]. The most straightforward approach is the combination of multiple InSAR LOS measurements from different SAR viewing geometries.

This approach of integrating multiple look directions has recently been extended into three-dimensional deformation monitoring of bridges [31], however, for direct comparison against ATS readings in a thermally responsive bridge, this approach has limitations since the observation period of the datasets are not exactly the same. If the acquisitions at different look angles are taken on different days or different times in the day, the bridge will be subjected to a different temperature, thus affecting the movement it experiences.

A first approximation of bridge movement in Section V-A assumed all movement was in one direction. Using a second line of sight direction would solve one further unknown. The concrete piers are each around 25m long (spanning the transverse length of the deck) and 0.7m thick (with an outer casing creating the appearance of a much wider section) and are considered stiff in the transverse direction. Using the reasonable structural assumption that the structure is rigid in the transverse direction, the LOS measurement in corresponding east and west sides of the bridge can be combined together, using acquisitions taken at the same temperature. This approach decomposes the LOS vector into longitudinal and vertical components (assuming zero transverse movement). However, this reduces the number of readings down to 10 instances when the east and west side had readings at the same temperature instance. This does not, however, ensure that the tidal loading was the same at each instance, which lowers the number of viable readings further.

### C. Multidimensional analysis

The time series of SAR signals associated with each corner reflector on the bridge identify a multidimensional signature of the linear transformations (e.g. translation, rotation) which the bridge may undergo as a result of various loading cases such as tidal movements, temperature expansion, live traffic load deformations and concrete shrinkage and creep. Point-by-point analysis involving first (e.g. average) and second (e.g. variance) order statistical measures may not be sufficient to investigate the accuracy of SAR signals being used to infer the same information as the measurements acquired by the ATS ground stations [32]. In fact, this approach might be affected by issues such as sparsity of data and complex data structures that could strongly degrade the characterization of the considered scenario. Moreover, undesired phenomena such as over-fitting and noise amplification induced by the nonlinear combination of the elements' scattering may not be efficiently tackled. As a result, the overall investigation results may be dramatically jeopardized and information loss might occur.

In order to provide a thorough investigation of the statistical and stochastic characteristics, a multidimensional approach exploring the manifold properties of the SAR and ATS measurements can be considered. Specifically, it is possible to understand the relationship between these measurements by taking into account the volume of the multidimensional subspace spanned by them. Indeed, it is worth recalling that a set of $R$ records characterised by $N$ attributes can be identified as a $N$-dimensional polytope [33]. According to a vertex geometry description of multidimensional datasets, every point living within the volume spanned by the $R$ records in this subspace can be characterised as a proper function of these $N$-dimensional samples [34], [35]. Thus, the volume spanned in a multidimensional space by a dataset provides relevant information on the properties of its own records. Moreover, it can be used to infer useful characteristics on similarities and regularities when comparing datasets.

In our case, it is possible to understand how accurately the SAR measurements can track and characterise the ground measurements by assessing the volumes spanned by their corresponding $N$-dimensional polytopes (where $N$ is the number of acquisitions), and then computing their ratio. In other terms, let R be the number of corner reflectors that are considered; moreover, let $\underline{a}_r = [a_{r_n}]_{n=1,\dots,N}$ and $\underline{s}_r = [s_{r_n}]_{n=1,\dots,N}$ be the ATS and SAR displacement measurements, respectively, associated with the $r$-th corner reflector location (i.e., $r \in \{1,\dots,R\}$). Every element in these vectors live in $\mathbb{R}$.

Then, let us define two $R \times N$ matrices $\underline{\underline{A}} = \{\underline{a}_r\}_{r=1,\dots,R}$ and $\underline{\underline{S}} = \{\underline{s}_r\}_{r=1,\dots,R}$. Thus, the volume spanned by the

ATS measurements $\underline{\underline{A}}$ (SAR measurements $\underline{\underline{S}}$) in the multidimensional space can be written as $V_A = \sqrt{|\det[\underline{\underline{A}}]|}$ ($V_S = \sqrt{|\det[\underline{\underline{S}}]|}$). Given the nature of the elements in $\underline{\underline{A}}$ and $\underline{\underline{S}}$, it is possible to prove that $V_A$ and $V_S$ are positive [33]. Furthermore, the aforementioned polytopes will cover a subspace in the $N$-dimensional space along the same directions [33]–[36]. Therefore, it is possible to assume that the ratio $\eta = V_S/V_A$ would provide useful insights on the representativeness of the ground measurements in terms of the SAR signals. Specifically, as $\eta \to 1$, we can expect that the SAR records would be carrying the same information of the ground measurements. Moreover, if $\eta > 1$, it is possible to state that the ground displacements can be identified and detailed by the SAR acquisitions. In the case considered here, the values of $\eta$ for the vertical and longitudinal component of the bridge displacements were 1.24 and 1.13, respectively.

Following this approach, we can understand how the SAR measurements could be used to describe the ground measurements, and quantify their effectiveness in this sense. To this aim, we can consider the SAR time series associated with each corner reflector as the extremal points of the aforesaid polytope that identify $\underline{\underline{S}}$. Hence, they represent a set of linear basis in the $N$-multidimensional space. Therefore, it is possible to write a generic $N$-dimensional vector $\phi$ as a combination of the SAR records. Specifically, it has been proven [37] that a polynomial combination of the basis induced by the extremal points can be used to characterise the linear and nonlinear effects occurring within the polytope.

Thus, $\phi$ can be approximated as a polynomial combination of $\underline{s}$, i.e., $\sum_{k=1}^{p}\sum_{r=1}^{R}\omega_{rk}\underline{s}_r^k$, where $\underline{s}_r^k = [s_{r_n}^k]_{(r,k)\in\{1,\dots,R\}\times\{1,\dots,p\}}$, $\omega_{rk}$ is the coefficient that weights the contribution of $\underline{s}_r$ for the $k$th order, and $p$ is the order of power of the non-linear contribution. Moreover, we can estimate the precision in characterizing the $\phi$ properties using the basis in $\underline{\underline{S}}$ by computing the Euclidean distance between $\phi$ and $\sum_{k=1}^{p}\sum_{r=1}^{R}\omega_{rk}\underline{s}_r^k$. Then, it is possible to assume that the ability of SAR to understand and quantify the actual displacements of the corner reflectors (that generate linear and nonlinear effects onto the SAR records) can be assessed by computing the reconstruction error that is achieved when approximating the ground measurements by means of the SAR measurements associated with each corner reflector as per the aforementioned approach. In detail, the reconstruction error (RE) can be written as follows:

$$RE = \sqrt{\frac{1}{RN}\sum_{l=1}^{R}||\underline{a}_l - \sum_{k=1}^{p}\sum_{r=1}^{R}\omega_{rkl}\underline{s}_r^k||^2} \tag{4}$$

RE identifies the coefficient that drives the $k$-th order contribution based on the $r$-th SAR measurement when approximating the $l$-th ground measurement. $\omega_{rkl}$ is the weighting of the $k$-th order contribution of the signal associated with the $r$-th corner reflector SAR measurement.

As such, $\omega_{rkl}$ is estimated by solving a linear programming problem where the minimization of RE is the objective function, with the sum-to-one and non-negativity constraints to be applied to the $\omega$ factors, i.e., $\sum_{r,k}\omega_{rkl} = 1$ and $\omega_{rkl} \geq 0$ $\forall(r,k,l)$ [37].

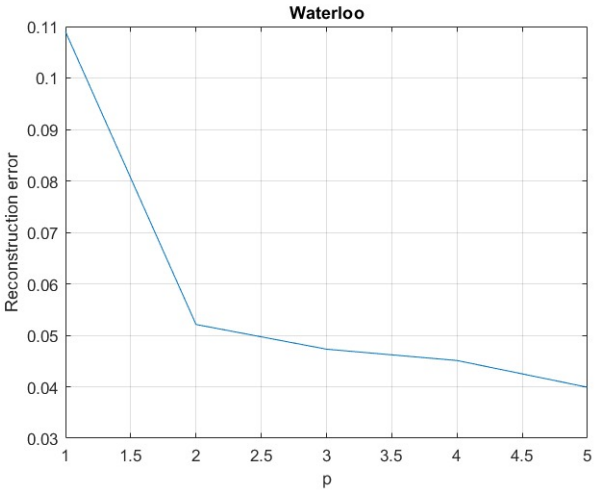


Fig. 12. Graph of possible Reconstruction Error (RE) values.

The value of $p = 1$ signifies a linear relation between the SAR and ATS readings, and higher values indicate higher order polynomial mapping between the two entities. The RE value decreases as we consider higher order non-linear combinations of the SAR signals to characterise what is shown by the ATS readings (Figure 12). This signifies the complicated relationship between the two entities, the SAR and ATS readings themselves, resulting from non-linear effects. This could include non-idealities associated with the non-perfect positioning of the ATS (i.e. the ATS is not fixed, which becomes a problem when the reference prisms cannot be relied upon). The next section explores this consideration and tries to quantify if and how the ATS position moves.

## VI. Method to combine terrestrial and SAR

Rather than considering the merits and disadvantages of each system, there is an opportunity to consider how the satellite measurements could be used to supplement the ATS measurements and resolve the unknown total station positions and other unknown quantities, giving a better insight into the absolute movements of the bridge (rather than the relative measurements derived from the data). The absolute displacement provides useful information to the bridge engineer. For Waterloo Bridge, knowledge on the absolute movements (rather than movements relative to one end of the bridge) would allow movements of the bridge to be distinguished from any movements of the abutments or approach viaducts. It should also be noted that such movements were not possible to measure by instrumenting with displacement gauges on the bridge itself either.

Let us consider the east readings for point $i$ at time $t$ and let us define its coordinates in a three dimensional space as $Ex_i^t$, $Ey_i^t$, and $Ez_i^t$. Then, it is possible to describe these quantities in terms of the corresponding ATS measurements (Figure 13) at each timestamp as follows:

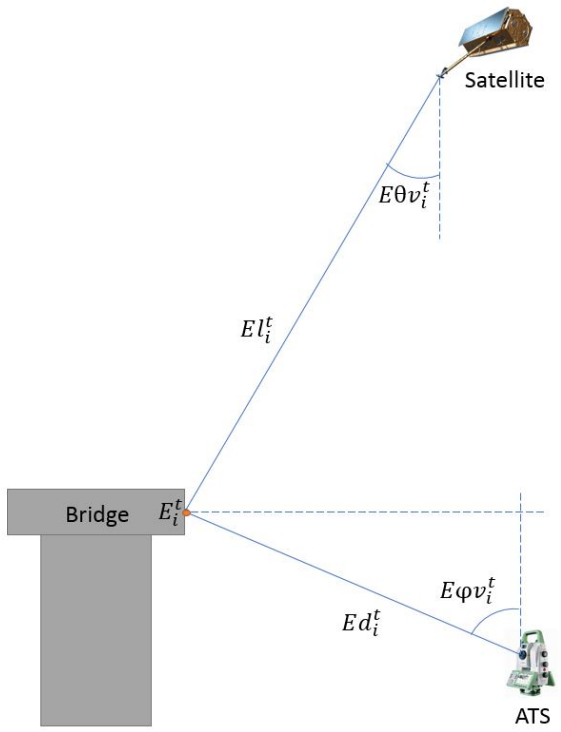


Fig. 13. ATS viewing geometry as used to define the equations in (5) and (6) for vertical movement in the z-direction. Diagrams are not drawn to scale.

$$\begin{aligned} Ex_i^t &= Ax^t + Ed_i^t \sin(E\varphi v_i^t)\cos(A\varphi^t + E\varphi h_i^t), \\ Ey_i^t &= Ay^t + Ed_i^t \sin(E\varphi v_i^t)\sin(A\varphi^t + E\varphi h_i^t), \\ Ez_i^t &= Az^t + Ed_i^t \cos(E\varphi v_i^t), \end{aligned} \quad (5)$$

where:

- $Ax^t$, $Ay^t$, and $Az^t$ identify the 3D coordinates of the ATS position at time $t$;
- $A\varphi^t$ is the reference angle used to compute the ATS measurements at time $t$;
- $Ed_i^t$ represents the distance between the $i$-th east point and ATS at time $t$;
- $E\varphi v_i^t$ and $E\varphi h_i^t$ are the vertical and horizontal angles measured from eastern point $i$ to $A\varphi^t$ at time $t$, respectively.

Analogously, it is possible to characterize $Ex_i^t$, $Ey_i^t$, and $Ez_i^t$ as functions of the satellite measurements (Figure 13) as follows:

$$\begin{aligned} Ex_i^t &= Sx^t + El_i^t \sin(E\theta v_i^t)\cos(E\theta h_i^t), \\ Ey_i^t &= Sy^t + El_i^t \sin(E\theta v_i^t)\sin(E\theta h_i^t), \\ Ez_i^t &= Sz^t - El_i^t \cos(E\theta v_i^t), \end{aligned} \quad (6)$$

where:

- $Sx^t$, $Sy^t$, and $Sz^t$ identify the 3D coordinates of the satellite position at time $t$: since the satellite position is assumed to be the same for every coherent acquisition, we can write $Sx^t = Sx$, $Sy^t = Sy$, and $Sz^t = Sz$ $\forall t$;
- $El_i^t$ represents the line-of-sight distance between satellite and the $i$-th east point at time $t$;
- $E\theta v_i^t$ and $E\theta h_i^t$ are the vertical and horizontal angles measured from eastern point $i$ to satellite line-of-sight at time $t$, respectively.

Hence, it is possible to extract information on the aforesaid unknown quantities in the system by considering the corresponding equations in (5) and (6). Thus, the following equations hold:

$$\begin{aligned} Ax^t - Ax^{t-1} &= El_i^t \sin(E\theta v_i^t)\cos(E\theta h_i^t) \\ &\quad - El_i^{t-1}\sin(E\theta v_i^{t-1})\cos(E\theta h_i^{t-1}) \\ &\quad + Ed_i^{t-1}\sin(E\varphi v_i^{t-1})\cos(A\varphi^{t-1} + E\varphi h_i^{t-1}) \\ &\quad - Ed_i^t \sin(E\varphi v_i^t)\cos(A\varphi^t + E\varphi h_i^t), \\ Ay^t - Ay^{t-1} &= El_i^t \sin(E\theta v_i^t)\sin(E\theta h_i^t) \\ &\quad - El_i^{t-1}\sin(E\theta v_i^{t-1})\sin(E\theta h_i^{t-1}) \\ &\quad + Ed_i^{t-1}\sin(E\varphi v_i^{t-1})\sin(A\varphi^{t-1} + E\varphi h_i^{t-1}) \\ &\quad - Ed_i^t \sin(E\varphi v_i^t)\sin(A\varphi^t + E\varphi h_i^t), \\ Az^t - Az^{t-1} &= El_i^{t-1}\cos(E\theta v_i^{t-1}) - El_i^t \cos(E\theta v_i^t) \\ &\quad + Ed_i^{t-1}\cos(E\varphi v_i^{t-1}) - Ed_i^t \cos(E\varphi v_i^t) \end{aligned} \quad (7)$$

Let us focus our attention on the vertical component of the ATS misplacement between two consecutive timestamps, i.e., $Az^t - Az^{t-1}$. Taking into account the readings obtained by considering two different points $i$ and $j$, it is possible to write:

$$\begin{aligned} &El_i^{t-1}\cos(E\theta v_i^{t-1}) - El_i^t \cos(E\theta v_i^t) \\ &+Ed_i^{t-1}\cos(E\varphi v_i^{t-1}) - Ed_i^t \cos(E\varphi v_i^t) = \\ &El_j^{t-1}\cos(E\theta v_j^{t-1}) - El_j^t \cos(E\theta v_j^t) \\ &+Ed_j^{t-1}\cos(E\varphi v_j^{t-1}) - Ed_j^t \cos(E\varphi v_j^t) \end{aligned} \quad (8)$$

Thus, since $E\theta v_i^t = E\theta v^t$ $\forall i$, it is possible to write:

$$\cos(E\theta v^{t-1}) = \alpha_{ij}^t \cos(E\theta v^t) + \beta_{ij}^t, \quad (9)$$

where $\alpha_{ij}^t = \frac{El_i^t - El_j^t}{El_i^{t-1} - El_j^{t-1}}$, whilst $\beta_{ij}^t = \tilde{\beta}_{ij}^t/(El_i^{t-1} - El_j^{t-1})$, and $\tilde{\beta}_{ij}^t = Ed_i^t\cos(E\varphi v_i^t) - Ed_i^{t-1}\cos(E\varphi v_i^{t-1}) + Ed_j^{t-1}\cos(E\varphi v_j^{t-1}) - Ed_j^t\cos(E\varphi v_j^t)$. Figure 14 plots this relationship over a number of different values.

Then, we can derive the analytical expression of $\cos(E\theta v^t)$ by taking into account the reading from point $k$, so that it is possible to write:

$$\cos(E\theta v^t) = \frac{\beta_{ij}^t - \beta_{ik}^t}{\alpha_{ij}^t - \alpha_{ik}^t}. \quad (10)$$

Once we replace the values described in (9) and (10) in the $Az^t - Az^{t-1}$ equation, we can retrieve the actual movement of the ATS on the vertical component, i.e., $\Delta z_{ATS}$.

Let us now take into account the $Ax^t - Ax^{t-1}$ difference. Assuming that $E\theta h_i^t = E\theta h^t$ $\forall i$ and bisection rules for trigonometric functions, it is possible to prove that the following equation holds:

$$
\begin{aligned}
(a_j^{t-1} - a_i^{t-1})\cos(E\theta h^{t-1}) \;=\; & (a_j^t - a_i^t)\cos(E\theta h^t) \\
& +(b_i^t - b_j^t)\cos(A\varphi^t) \\
& +(c_j^t - c_i^t)\sin(A\varphi^t) \\
& +(b_j^{t-1} - b_i^{t-1})\cos(A\varphi^{t-1}) \\
& +(c_i^{t-1} - c_j^{t-1})\sin(A\varphi^{t-1}),
\end{aligned} \tag{11}
$$

where the $a$, $b$ and $c$ coefficients are defined as follows:

- $a_i^t = El_i^t \sin(E\theta v^t)$;
- $b_i^t = Ed_i^t \sin(E\varphi v_i^t)\cos(E\varphi h_i^t)$;
- $c_i^t = Ed_i^t \sin(E\varphi v_i^t)\sin(E\varphi h_i^t)$.

Then, we can define $\cos(E\theta h^t)$ as follows:

$$
\begin{aligned}
(A_{ij} - A_{ik})\cos(E\theta h^t) \;=\; & (B'_{ik} - B'_{ij})\cos(A\varphi^t) \\
& +(C'_{ik} - C'_{ij})\sin(A\varphi^t) \\
& +(B''_{ik} - B''_{ij})\cos(A\varphi^{t-1}) \\
& +(C''_{ik} - C''_{ij})\sin(A\varphi^{t-1}),
\end{aligned} \tag{12}
$$

where

- $A_{ij} = (a_j^t - a_i^t)/(a_j^{t-1} - a_i^{t-1})$;
- $B'_{ij} = (b_i^t - b_j^t)/(a_j^{t-1} - a_i^{t-1})$;
- $B''_{ij} = (b_i^{t-1} - b_j^{t-1})/(a_j^{t-1} - a_i^{t-1})$;
- $C'_{ij} = (c_i^t - c_j^t)/(a_j^{t-1} - a_i^{t-1})$;
- $C''_{ij} = (c_i^{t-1} - c_j^{t-1})/(a_j^{t-1} - a_i^{t-1})$.

Finally, it is possible to write:

$$
R'_{ijkm}\cos(A\varphi^t - \Delta'_{ijkm}) = R''_{ijkm}\cos(A\varphi^{t-1} - \Delta''_{ijkm}), \tag{13}
$$

where the $R'$, $R''$, $\Delta'$ and $\Delta''$ parameters are defined as follows:

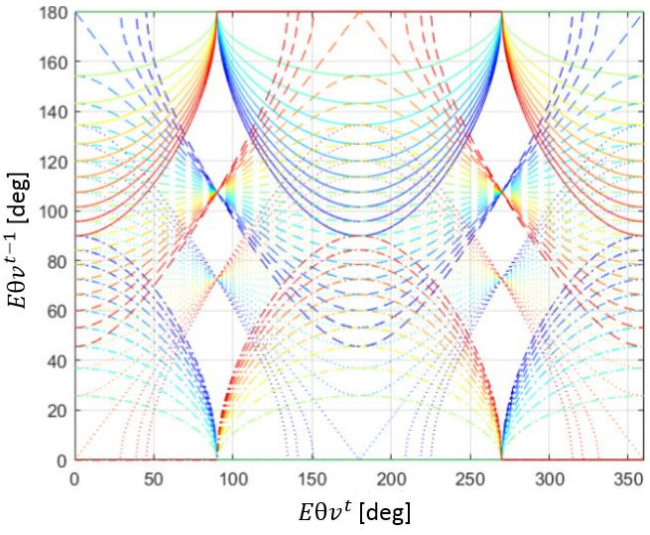


Fig. 14. $E\theta v^{t-1}$ as a function of $E\theta v^t$, $\alpha_{ij}^t$, and $\beta_{ij}^t$ as in (9). The different set-ups of $\alpha_{ij}^t$ and $\beta_{ij}^t$ are represented in terms of different line colours and styles, respectively. Specifically, the colours from blue to red represent values of $\alpha_{ij}^t$ ranging from -1 to 1. Solid lines, dashed lines, point lines, and dash-point lines identify $\beta_{ij}^t = \{-1, -0.5, 0.5, 1\}$, respectively.

- $R'_{ijkm} = \sqrt{(D'_{ijk} - D'_{ijm})^2 + (E'_{ijk} - E'_{ijm})^2}$;
- $R''_{ijkm} = \sqrt{(D''_{ijk} - D''_{ijm})^2 + (E''_{ijk} - E''_{ijm})^2}$;
- $\Delta'_{ijkm} = \arctan[(E'_{ijm} - E'_{ijk})/(D'_{ijk} - D'_{ijm})]$;
- $\Delta''_{ijkm} = \arctan[(E''_{ijm} - E''_{ijk})/(D''_{ijk} - D''_{ijm})]$;
- $D'_{ijk} = (B'_{ik} - B'_{ij})/(A_{ij} - A_{ik})$;
- $D''_{ijk} = (B''_{ik} - B''_{ij})/(A_{ij} - A_{ik})$;
- $E'_{ijk} = (C'_{ik} - C'_{ij})/(A_{ij} - A_{ik})$;
- $E''_{ijk} = (C''_{ik} - C''_{ij})/(A_{ij} - A_{ik})$.

Three prism/corner locations were used to understand vertical (z) positioning. Figure 15 plots the $\Delta z_{ATS}$ results according to the data collected on Waterloo bridge from January to December 2018, and thus provides insight into the movement of the ATS device location itself during the period of measurement. This figure displays what appears to be a large spike in the measurement, but on closer inspection shows a movement of only 2mm, with the other measurements being significantly smaller (sub-millimeter). The ATS was installed at this location on the assumption that the foundation layout would limit movement in that area, and this is confirmed by the movements shown in this figure.

The equations outlined can also be used to determine the x and y positions, but in these directions 5 prism/corner locations would have to be considered (rather than 3 used to work out the z-direction position).

## VII. Conclusions

The topic of InSAR time series measurement for application to bridges was presented in this paper. Small scale corner reflectors were trialled and key points on the bridge were monitored over time using both InSAR and ATS measurements for comparison. Measurements were found to be comparable when comparing relative movement of points along the bridge from one another. The limited frequency of satellite readings and noise within readings means that it is not a technique that could replace traditional monitoring methods, but more seasonal trends can be tracked, and there is an opportunity to complement traditional inspection regimes with additional insights.

The relationship between SAR and ATS readings was explored using multidimensional analysis to understand how accurately the SAR measurements could track and characterise the ATS readings. It was found that the two readings were directly related such that they could be mapped, but the nature of the transformation was highly non-linear. The overall plots of relationship indicate that SAR data can be used as a reasonable indication of bridge movement, but some irregularities must be further explored for full confidence. Finally a combination of ATS and SAR readings can be used together to determine unknown positions and uncertainties.

There are a number of satellites currently available with free and commercial data. Free data from constellations such as Sentinel 1 do not provide sufficient resolution to study the behavior of smaller bridges such as Waterloo. TerraSAR-X stripmap resolution is able to image more detail but comes at cost. This cost depends on several factors (including supplier and quantity) but for a study such as the one conducted

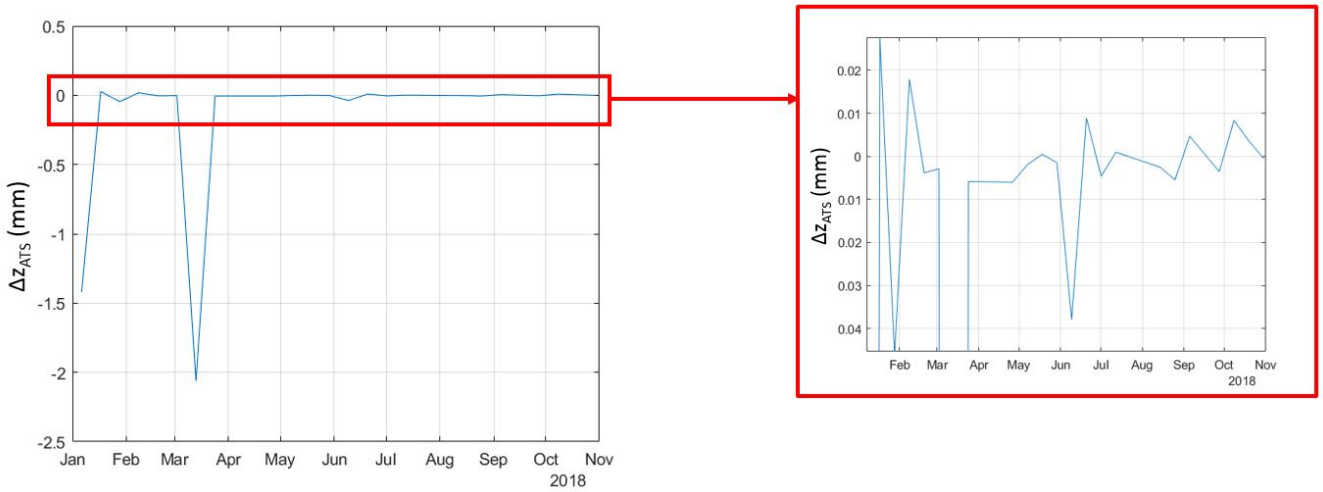


Fig. 15. Misplacement of ATS on the vertical direction $\Delta z_{ATS} = Az^t - Az^{t-1}$ computed according to (8), (9), and (10).

this cost rises to tens of thousands of dollars. However, the assessment of financial value must be compared with not just the cost of ATS devices, but also the associated costs. These include power supply, maintenance and manual servicing, potential road closures and disruptions. The value of each of these can also reach tens of thousands of dollars. The actual added 'value' of such measurements must be assessed by an asset owner in the context of some of these considerations (and perhaps on the possibility of spreading the cost over a number of assets within a single image) and it may only be worthwhile as the price point for images decreases or readings become more frequent to pick up daily variations in behavior.

Future works will address multisensor remote sensing data analysis to increase the ability of obtaining information on urban structures from low resolution sensing constellations, as well as to improve the temporal resolution for understanding dynamic processes on Earth surface affecting the considered structures.

## APPENDIX
## TERRASAR-X ACQUISITION LIST

Refer to Table 1. All acquisitions have an incidence angle range of 36.11 - 38.5 degrees. Ascending acquisitions were taken at 17:44 and descending acquisitions were taken at 06:17.

TABLE I
TERRASAR-X ACQUISITION LIST

| Ascending Acquisition Dates | Descending Acquisition Dates |
|---|---|
| 18-DEC-2017 | 15-DEC-2017 |
| 29-DEC-2017 | 26-DEC-2017 |
| 09-JAN-2018 | 06-JAN-2018 |
| 20-JAN-2018 | 17-JAN-2018 |
| 31-JAN-2018 | 28-JAN-2018 |
| 11-FEB-2018 | 08-FEB-2018 |
| 22-FEB-2018 | 19-FEB-2018 |
| 05-MAR-2018 | 02-MAR-2018 |
| 16-MAR-2018 | 13-MAR-2018 |
| 27-MAR-2018 | 24-MAR-2018 |
| 07-APR-2018 | 04-APR-2018 |
| 18-APR-2018 | 26-APR-2018 |
| 29-APR-2018 | 07-MAY-2018 |
| 10-MAY-2018 | 18-MAY-2018 |
| 21-MAY-2018 | 29-MAY-2018 |
| 01-JUN-2018 | 09-JUN-2018 |
| 12-JUN-2018 | 20-JUN-2018 |
| 23-JUN-2018 | 01-JUL-2018 |
| 04-JUL-2018 | 12-JUL-2018 |
| 15-JUL-2018 | 23-JUL-2018 |
| 26-JUL-2018 | 03-AUG-2018 |
| 06-AUG-2018 | 14-AUG-2018 |
| 17-AUG-2018 | 25-AUG-2018 |
| 28-AUG-2018 | 05-SEP-2018 |
| 08-SEP-2018 | 16-SEP-2018 |
| 19-SEP-2018 | 27-SEP-2018 |
| 30-SEP-2018 | 08-OCT-2018 |
| 11-OCT-2018 | 19-OCT-2018 |
| 22-OCT-2018 | 30-OCT-2018 |
| 02-NOV-2018 | 10-NOV-2018 |

## ACKNOWLEDGMENT

The authors would firstly like to express their thanks to Westminster City Council who kindly provided permission and support for this research and FM Conway who supported this work by carrying out installations on site. This work was made possible by EPSRC (UK) Award 1636878, with iCase sponsorship from the National Physical Laboratory and additional funding from Laing O'Rourke. This work is also funded in part by the Centre for Integrated Remote Sensing and Forecasting for Arctic Operations (CIRFA) and the Research Council of Norway (RCN Grant no. 237906). TerraSAR-X satellite data was purchased by the Satellite Application Catapult through grant funding provided by Innovate UK. The authors would also like to thank Finite Element Analysis Ltd for providing

a licence for their LUSAS software and Laing O'Rourke for additional surveying information.

## REFERENCES


[1] M.; Moore, B.; Phares, B.; Graybeal, R.; Dennis, and G. Washer, "Reliability of Visual Inspection for Highway Bridges , Volume I : Final Report," Tech. Rep. FHWA-RD-01-020, U.S. Department of Transport, McLean, VA, 2001.

[2] F.C. Lea and C. R. Middleton, "Reliability of Visual Inspection for Highway Bridges," Tech. Rep. CUED/D-STRUCT/TR. 201, Department of Engineering, University of Cambridge, Cambridge, 2002.

[3] Welsh Government The Highways Agency, Transport Scotland and The Department for Regional Development Northern Ireland, "Inspection of Highway Structures," Tech. Rep., 2007.

[4] S.G. McRobbie, M.A. Wright, and A. Chan, "Can technology improve routine visual bridge inspections ?," *Proceedings of the ICE - Bridge Engineering*, vol. 168, no. BE3, pp. 197–207, 2015.

[5] J. Bennetts, P.J. Vardanega, C.A. Taylor, and S.R. Denton, "Bridge data - What do we collect and how do we use it?," in *Proceedings of the International Conference on Smart Infrastructure and Construction*, Cambridge, UK, 2016, pp. 531–536, ICE Publishing.

[6] Richard Bamler and Philipp Hartl, "Synthetic aperture radar interferometry," *Inverse Problems*, vol. 14, no. 4, pp. 1–54, 1998.

[7] Alessandro Ferretti, Claudio Prati, and Fabrio Rocca, "Permanent Scatters in SAR Interferometry," *IEEE Transactions on Geoscience and Remote Sensing*, vol. 39, no. 1, pp. 8–20, 2001.

[8] Alberto Moreira, Pau Prats-Iraola, Marwan Younis, Gerhard Krieger, Irena Hajnsek, and Konstantinos P Papathanassiou, "A Tutorial on Synthetic Aperture Radar," *IEEE Geoscience and Remote Sensing Magazine*, pp. 6–43, 2013.

[9] Francesca Cigna, Rosa Lasaponara, Nicola Masini, Pietro Milillo, and Deodato Tapete, "Persistent scatterer interferometry processing of COSMO-skymed stripmap HIMAGE time series to depict deformation of the historic centre of Rome, Italy," *Remote Sensing*, vol. 6, no. 12, pp. 12593–12618, 2014.

[10] Kui Yang, Li Yan, Guoman Huang, Chu Chen, Zhengpeng Wu, and Jonathan Li, "Monitoring Building Deformation with InSAR: Experiments and Validation," 2016.

[11] Alexander Schunert and Uwe Soergel, "Assignment of Persistent Scatterers to Buildings," *IEEE Transactions on Geoscience and Remote Sensing*, vol. 54, no. 6, pp. 3116–3127, 2016.

[12] Batuhan Osmanoğlu, Timothy H. Dixon, Shimon Wdowinski, Enrique Cabral-Cano, and Yan Jiang, "Mexico City subsidence observed with persistent scatterer InSAR," *International Journal of Applied Earth Observation and Geoinformation*, vol. 13, no. 1, pp. 1–12, 2011.

[13] D. L. Galloway, K. W. Hudnut, S. E. Ingebritsen, S. P. Phillips, G. Peltzer, F. Rogez, and P. A. Rosen, "Detection of aquifer system compaction and land subsidence using interferometric synthetic aperture radar, Antelope Valley, Mojave Desert, California," *Water Resources Research*, vol. 34, no. 10, pp. 2573–2585, 1998.

[14] Zbigniew Perski, Ramon Hanssen, Antoni Wojcik, and Tomasz Wojciechowski, "InSAR analyses of terrain deformation near the Wieliczka Salt Mine, Poland," *Engineering Geology*, vol. 106, no. 1, pp. 58–67, 2009.

[15] Jonny Rutqvist, Donald W. Vasco, and Larry Myer, "Coupled reservoir-geomechanical analysis of CO2 injection and ground deformations at In Salah, Algeria," *International Journal of Greenhouse Gas Control*, vol. 4, no. 2, pp. 225–230, 2010.

[16] Giovanni Barla, Andrea Tamburini, Sara Del Conte, and Chiara Giannico, "InSAR monitoring of tunnel induced ground movements," *Geomechanik und Tunnelbau*, vol. 9, no. 1, pp. 15–22, 2016.

[17] Daniele Perissin, Zhiying Wang, and Hui Lin, "Shanghai subway tunnels and highways monitoring through Cosmo-SkyMed Persistent Scatterers," *ISPRS Journal of Photogrammetry and Remote Sensing*, vol. 73, pp. 58–67, 2012.

[18] Esra Erten and Cristian Rossi, "The worsening impacts of land reclamation assessed with Sentinel-1: The Rize (Turkey) test case," *International Journal of Applied Earth Observation and Geoinformation*, vol. 74, pp. 57–64, 2019.

[19] Michele Crosetto, Oriol Monserrat, María Cuevas-González, Núria Devanthéry, and Bruno Crippa, "Persistent Scatterer Interferometry: A review," *ISPRS Journal of Photogrammetry and Remote Sensing*, vol. 115, pp. 78–89, 2016.

[20] Gianfranco Fornaro, Diego Reale, and Simona Verde, "Monitoring thermal dilations with millimetre sensitivity via multi-dimensional SAR imaging," in *Proceedings of the 2012 Tyrrhenian Workshop on Advances in Radar and Remote Sensing (TyWRRS)*, Naples, Italy, 2012, pp. 131–135, IEEE.

[21] Milan Lazecky, Ivana Hlavacova, Matus Bakon, Joaquim J. Sousa, Daniele Perissin, and Gloria Patricio, "Bridge Displacements Monitoring Using Space-Borne X-Band SAR Interferometry," *IEEE Journal of Selected Topics in Applied Earth Observations and Remote Sensing*, vol. 10, no. 1, pp. 205–210, 2017.

[22] J. J. Sousa and L. Bastos, "Multi-temporal SAR interferometry reveals acceleration of bridge sinking before collapse," *Natural Hazards and Earth System Science*, vol. 13, no. 3, pp. 659–667, 2013.

[23] Sivasakthy Selvakumaran, Simon Plank, Christian Geiß, Cristian Rossi, and Campbell Middleton, "Remote monitoring to predict bridge scour failure using Interferometric Synthetic Aperture Radar (InSAR) stacking techniques," *International Journal of Applied Earth Observation and Geoinformation*, vol. 73, no. April, pp. 463–470, 2018.

[24] E.J. Buckton and J. Cuerel, "The New Waterloo Bridge," *Journal of the Institution of Civil Engineers*, vol. 20, no. 7, pp. 145–178, 1943.

[25] Kamal Sarabandi and Tsen Chieh Chiu, "Optimum corner reflectors for calibration of imaging radars," *IEEE Transactions on Antennas and Propagation*, vol. 44, no. 10, pp. 1348–1361, 1996.

[26] Paul A Rosen, Scott Hensley, Ian R Joughin, Fuk K Li, Søren N Madsen, Ernesto Rodríguez, and Richard M Goldstein, "Synthetic Aperture Radar Interferometry," *Proceedings of the IEEE*, vol. 88, no. 3, pp. 334–382, 2000.

[27] P. Berardino, G. Fornaro, R. Lanari, and E. Sansosti, "A new algorithm for surface deformation monitoring based on small baseline differential SAR interferograms," *IEEE Transactions on Geoscience and Remote Sensing*, vol. 40, no. 11, pp. 2375–2383, 11 2002.

[28] Stefan Matthias Gernhardt, *High Precision 3D Localization and Motion Analysis of Persistent Scatterers using Meter-Resolution Radar Satellite Data*, Ph.D. thesis, Technical University of Munich, 2012.

[29] Xiaoqiong Qin, Mingsheng Liao, Mengshi Yang, and Lu Zhang, "Monitoring structure health of urban bridges with advanced multi-temporal InSAR analysis," *Annals of GIS*, vol. 23, no. 4, pp. 293–302, 2017.

[30] J. Hu, Z. W. Li, X. L. Ding, J. J. Zhu, L. Zhang, and Q. Sun, "Resolving three-dimensional surface displacements from InSAR measurements: A review," *Earth-Science Reviews*, vol. 133, pp. 1–17, 2014.

[31] Xiaoqiong Qin, Xiaoli Ding, and Mingsheng Liao, "Three-Dimensional Deformation Monitoring and Structural Risk Assessment of Bridges by Integrating Observations from Multiple SAR Sensors," in *IEEE International Geoscience and Remote Sensing Symposium (IGARSS)*, Valencia, Spain, 2018, pp. 1384–1387, IEEE.

[32] Stephen Boyd and Lieven Vandenberghe, *Convex Optimization*, Cambridge University Press, Cambridge, UK, 2004.

[33] V. Kaibel and A. Schwartz, "On the complexity of polytope isomorphism problems," *Graphs and Combinatorics*, vol. 19, no. 2, pp. 215–230, 2003.

[34] V. Prasolov, *Problems and Theorems in Linear Algebra*, American Mathematical Society, Providence, U.S., 1st edition, 1994.

[35] Glen E. Bredon, *Topology and Geometry*, vol. 91, Springer, New York, U.S., 2017.

[36] G. H. Golub and C. F. Van Loan, "Matrix Computations," *The Mathematical Gazette*, vol. 74, no. 469, pp. 322, 1990.

[37] Andrea Marinoni and Paolo Gamba, "A novel approach for efficient P-Linear hyperspectral unmixing," *IEEE Journal on Selected Topics in Signal Processing*, vol. 9, no. 6, pp. 1156–1168, 2015.